THE JOURNAL OF PHYSICAL CHEMISTRY C
A JOURNAL OF THE AMERICAN CHEMICAL SOCIETY

pubs.acs.org/JPCC
Article

Label-Free Anti-Brownian Trapping of Single Nanoparticles in Solution

Published as part of The Journal of Physical Chemistry C special issue "Photothermal and Non-Fluorescent Imaging in Microscopy and Spectroscopy".

William B. Carpenter, Abhijit A. Lavania, Allison H. Squires, and W. E. Moerner*

Cite This: https://doi.org/10.1021/acs.jpcc.4c05878
Read Online

ABSTRACT: Today, biomolecular nanoparticles are prevalent as diagnostic tools and molecular delivery carriers, and it is particularly useful to examine individuals within a sample population to quantify the variations between objects and directly observe the molecular dynamics involving these objects. Using interferometric scattering as a highly sensitive label-free detection scheme, we recently developed the interferometric scattering anti-Brownian electrokinetic (ISABEL) trap to hold a single nanoparticle in solution for extended optical observation. In this perspective, we describe how we implemented this trap, how it extends the capabilities of previous ABEL traps, and how we have begun to study individual carboxysomes, a fascinating biological carbon fixation nanocompartment. By monitoring single nanocompartments for seconds to minutes in the ISABEL trap using simultaneous interferometric scattering and fluorescence spectroscopy, we have demonstrated single-compartment mass measurements, cargo-loading trends, and redox sensing inside individual particles. These experiments benefit from rich multiplexed correlative measurements utilizing both scattering and fluorescence with many exciting future capabilities within reach.

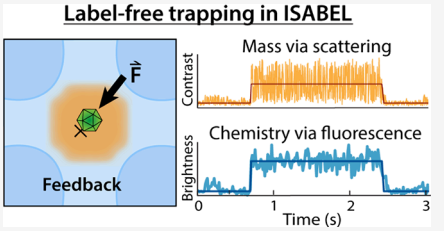

1. INTRODUCTION

Nanoparticles are increasingly being engineered and employed to carry out precise functions such as enhancing detection sensitivity of target molecules,[1] drug delivery,[2] heterogeneous catalysis,[3] reaction engineering,[4] single-photon emission,[5] and quantum sensing.[6] While particle uniformity is typically desired, a sample can display various forms of structural or kinetic heterogeneity, e.g., in terms of chemical reactivity or photophysical dynamics.[7] These heterogeneities can reveal fascinating behavior about particle assembly, but a population of abnormal particles can result in limited efficacy in the desired application.[2] As a result, it is important and illuminating to observe individual nanoparticles to uncover distributions of properties and monitor dynamics. Here, we focus on individual particles in solution with emphasis on size and optical properties. Solution-based monitoring techniques include dynamic light scattering (DLS),[8] fluorescence correlation spectroscopy,[9] and nanoparticle tracking analysis (NTA),[10] which enable hydrodynamic sizing and minimize perturbations to delicate biomolecular systems. However, these measurements are either ensemble-averaged[11,12] or have difficulty detecting scattering intensity from particles smaller than ∼50 nm.[10,13,14] In all of these cases, rare processes or dynamics with long characteristic timescales (seconds−minutes) are inaccessible for these solution-based measurement techniques.

To control the position of a single particle in solution, anti-Brownian electrokinetic (ABEL) trapping was developed[15] (along with other trapping schemes[16,17]), which implements a negative feedback loop on a particle's position to hold it in solution for extended periods of time. Briefly, the position of a fluorescent object is rapidly estimated, and feedback forces guide the particle back to the center of a trapping region to counteract Brownian motion (further details in Section 2).[16] Since the initial demonstration in 2006,[15] ABEL trapping has allowed the extended monitoring and dynamical study of numerous individual molecular systems such as bacteriophage λ-DNA,[18] chaperonin proteins,[19] and a variety photosynthetic complexes and assemblies.[20−24] More recently, ABEL trapping has produced high-precision and highly multiplexed single-molecule FRET sensing.[25,26] Additionally, the fluorescence sensitivity, efficient position estimation, and a rapid feedback loop even allow the trapping of single fluorophores in solution.[27,28] Extended monitoring also enables multiple simultaneous spectroscopic and transport readouts from a

Received: August 30, 2024
Revised: October 31, 2024
Accepted: November 6, 2024

single object, including the fluorescence brightness, fluorescence lifetime, emission spectrum, diffusion coefficient, and electrokinetic mobility.[24,29]

While ABEL trapping was among the earliest solution-phase techniques for extended single-particle observation, many other methods now extend our capabilities for single-molecule trapping in a variety of configurations and contexts.[17] Real-time 3D single-particle tracking (RT-3D-SPT)[30] introduces feedback to the microscope stage's position to track individual nanoparticles in complicated environments. This allows relatively deep axial observation and direct observation of particle migration such as of a virus landing on a cell membrane.[31] For high-throughput and parallelized single-molecule trapping, convex-lens induced confinement (CLiC) microscopy[32] physically traps single molecules and nanoparticles in a microwell array with the additional ability to flow in new analytes or buffers.[33,34] Label-free, passive feedback schemes such as geometry-induced electrostatic trapping,[35] thermophoretic trapping,[36] self-induced back action,[37] and plasmonically enhanced optical tweezers in metallic nanoapertures[38] allow for particle trapping and extended observation on objects that are not fluorescently labeled. However, for the strategies described above that rely on fluorescence observation, long-term monitoring is still limited by fluorophore bleaching or blinking, and nanoplasmonic devices require close proximity to locally enhanced optical fields.

Label-free observation has revolutionized single-nanoparticle detection in the past two decades. In particular, the phenomenon of interferometric scattering (known as iSCAT[39] or IRIS[40]) amplifies single-particle scattering by homodyning the scattering signal with a local oscillator reflection at the interface between the buffer and cover glass.[41] A key benefit of this homodyning is the approximate scaling of the interferometric scattering signal with the particle volume versus squared-volume scaling for dark-field scattering, described more precisely below. This has opened up a variety of applications in particle detection and imaging, such as optical detection of 5 nm gold nanoparticles,[42] optical mass measurements of single proteins,[43] single-particle tracking with composition sensitivity,[44,45] single-protein detection[43] and diffusional observation,[46−50] and even label-free whole-cell imaging.[51,52] A recent approach using a combination of forward- and backscattered light has enabled estimation of the single-particle effective radius and aspherical geometry, adding new measurement dimensions to label-free techniques.[53]

The label-free nature of interferometric scattering detection provides a mechanism to further expand the systems and observables amenable to anti-Brownian trapping. By shifting particle detection from fluorescence to the universal phenomenon of interferometric scattering, a broader range of sample types can be localized and thus be trapped. Importantly, interferometric scattering can, in principle, provide indefinite trapping time without the blinking or photobleaching complications seen in fluorescence. Moreover, scattering's sensitivity to an object's refractive index and volume provides new measurement axes to characterize single objects and assess for heterogeneity. Finally, with careful choice of the scattering wavelength, it is feasible to still incorporate fluorophores for their spectroscopic reporting ability, retaining the benefits of the information-rich multiplexed readout of the ABEL trap with more flexibility in the types of fluorescence reporters that can be used.

In this review, we summarize the first few experiments that have demonstrated the capabilities of the newly developed interferometric scattering ABEL (ISABEL) trap. We first present the principles of electrokinetic feedback as implemented with fluorescence in the ABEL trap and then describe scattering detection and the particular needs for using interferometric scattering to estimate a position for feedback. We also describe how scattering contrast can be calibrated to determine a particle's scattering cross section and how we have also incorporated simultaneous fluorescence monitoring. We then demonstrate trapping on an ∼100 nm bacterial nanocompartment called the carboxysome, revealing how the ISABEL trap can be used to measure single-object masses (here, in MDa) and how carboxysome loading can be characterized with a core-localized fluorescent reporter. We then present a study where we introduced a redox-sensitive green fluorescent protein (GFP) mutant to sense the redox environment inside individual carboxysomes, allowing us to monitor the permeation kinetics of small (300 Da) reductants into carboxysome interiors. Finally, we conclude with an outlook for potential future directions with this methodology. These initial experiments demonstrate how anti-Brownian trapping can reveal exquisite detail from a single biomolecular nanoparticles, enabling a whole host of new experiments on these types of systems.

2. IMPLEMENTATION OF AN INTERFEROMETRIC SCATTERING ABEL (ISABEL) TRAP

We first review the key features of an ABEL trap: electrokinetic feedback forces (provided by DC voltages) are applied to the solution to directly counteract random Brownian movements extracted from a 2D confocal fluorescence image (Figure 1). When the feedback is off, particles diffuse randomly through the excitation and trapping region, producing random short bursts of signal on a photodetector (Figure 1a, left). When feedback is on, the particle's position only slightly fluctuates around the center of the trap and provides steady fluorescence output (Figure 1a, right). To trap a particle, the particle position must be continuously monitored, and feedback forces are applied to restore the particle position toward the center of the trap in a closed-loop feedback scheme (Figure 1b).

In the typical implementation of an ABEL trap, a quartz microfluidic cell positioned atop an inverted microscope holds dilute (∼pM) samples, which are excited by a confocal beam rapidly scanned across a shallow trapping region (∼700 nm height, ∼2 μm × 2 μm). When a single particle enters the trapping region, fluorescence is collected with a high-NA objective and sent to one or more avalanche photodiodes (APDs) for photon-by-photon detection. The arrival of each photon is converted to a new position estimate according to the scan pattern and calibrated lag, and a Kalman filter provides an updated estimate of the particle position. Two pairs of electrodes positioned along the x and y axes of the microfluidic cell apply computer-controlled closed-loop feedback voltages, which provide electric fields to move the particle back toward the center of the trap either by electrophoresis (Figure 1c) or electro-osmosis (Figure 1d), as previously described.[27] The electrokinetic nature of the feedback forces enables fast feedback and the trapping of even single molecules if detection can be sufficiently fast and sensitive.

The key difference between an ISABEL trap and a regular ABEL trap is that in an ISABEL trap, interferometric scattering rather than fluorescence is used to localize the trapped particle

https://doi.org/10.1021/acs.jpcc.4c05878
J. Phys. Chem. C XXXX, XXX, XXX−XXX

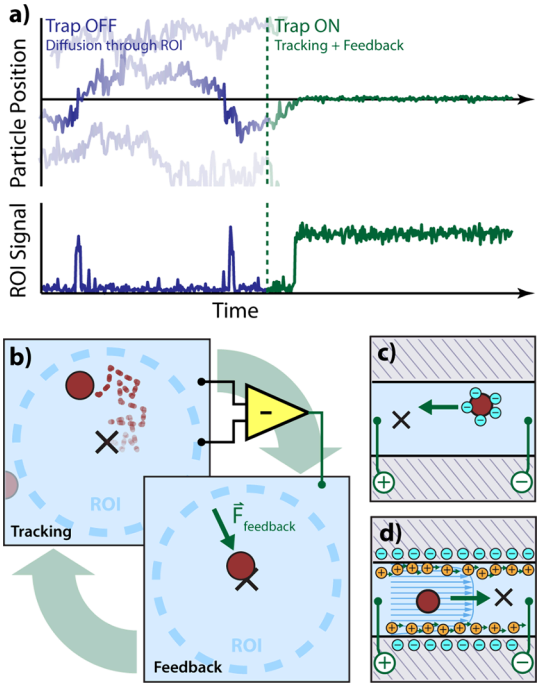

Figure 1. (a) Illustration of the position and signal of simulated diffusing fluorescent particles in and near the region of interest (ROI) when trapping feedback is off (left, blue) and on (right, green; only one particle is selected). (b) Principle of closed-loop feedback for ABEL trapping (top view). (c) Electrophoretic and (d) electro-osmotic feedback forces (side view) can move the particle toward the trap center. Figure adapted with permission from ref 16. Copyright 2018 Springer.

(Figure 2a). Illumination and detection paths for scattered laser light are p- and s-polarized, respectively, and are separated by using a polarizing beam splitter and quarter waveplate so that circularly polarized light illuminates the sample (Figure 2a, bottom right). In contrast to many wide-field iSCAT setups, in an ISABEL trap, the illumination laser is scanned in a confocal geometry using a pair of acousto-optic deflectors (AODs) to generate an iSCAT signal on a point detector with spatiotemporal information faster than sCMOS or EMCCD scientific cameras (Figure 2b). When the trapped particle is present within the incoming illumination field, E_i, a scattered field E_s is generated from interaction with the particle according to its size and the complex polarizability of the material. Ideally, the primary reference field, E_r, is provided by the reflection from the coverslip−water interface due to a short coherence length of the excitation laser (Figure 2c). In practice, reflections from other nearby interfaces, such as the upper water−quartz interface or quartz−air interface, may also contribute to the detected iSCAT signal. The detected signal intensity, I_{det}, depends on both E_r and E_s and their relative phase θ:

$$I_{det} \propto |E_r + E_s|^2 = |E_r|^2 + 2|E_r||E_s|\cos\theta + |E_s|^2 \quad (1)$$

Note that a particle will exhibit position-dependent θ as it explores the trap in x, y, and z.

The photodiode signals from the combined scattered and reference fields at each illumination beam position, S_{det}, reveal the location of the particle by comparison (flat-fielding) with a background scan, S_{bkg}, in which no particle is present. The absolute fractional scattering contrast after flat-fielding, C_f, at each point is then calculated as (note that the absolute value maintains a positive sign needed for feedback):

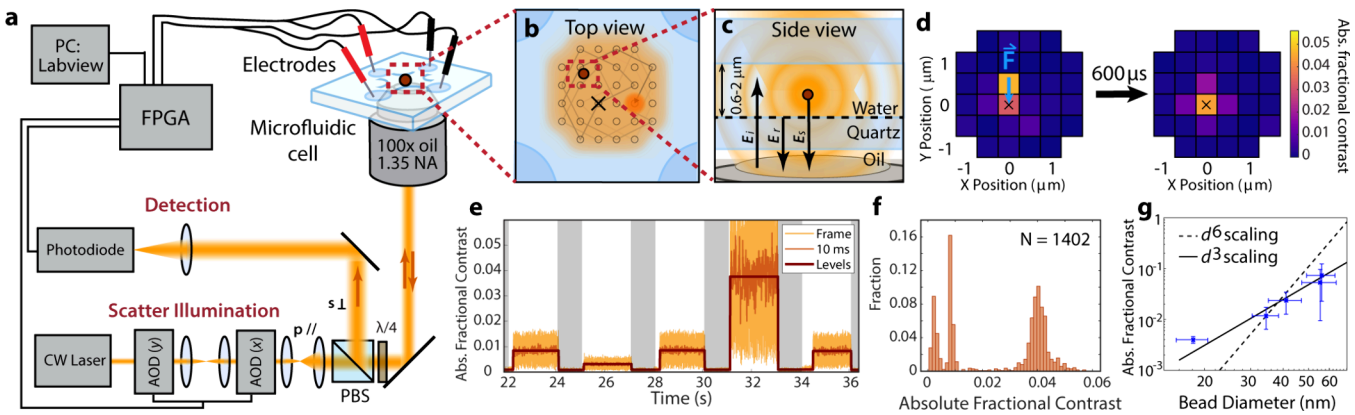

Figure 2. ISABEL trap overview. (a) Schematic of the ISABEL trap layout. Laser: orange. Hardware: gray. Microfluidic cell: light blue. Electrodes: red and black. Trapped particle: maroon. (b) Top view of the ISABEL 32-point illumination grid (orange), showing the knight's tour scan pattern (arrows, gray circles), the trap center (black x), and the particle position (maroon). (c) Side view of a particle in the ISABEL microfluidic cell, showing incident (E_i) and scattered (E_s) fields along with the reference field (E_r). (d) Flat-fielded representation of interferometric scattering data from the ISABEL trap, showing the point of highest contrast at the location of the particle. Left: The particle is located toward +y relative to the trap center (black x), resulting in application of a restoring force (cyan F) on the electrodes. Right: On the next update loop, the applied feedback successfully returned the particle position to coincide with the trap center. (e) Raw and filtered data from a working ISABEL trap. Particles from a mixture of 20, 30, and 50 nm gold beads are observed to enter the trap one at a time when feedback is on (white background), causing a sharp step up in scattering contrast (orange). Contrast remains high during trapping and returns to the background level upon switching off the feedback (gray background). The darker orange trace has been filtered at 100 Hz; the bold brown trace denotes the values of maximum-likelihood-estimated levels for each trapping event. (f) Fractional contrast for each trapping event should correspond to particle size; an all-particles histogram of the data from panel (e) illustrates three distinct peaks. (g) Peak positions for gold nanoparticles of known diameter (blue x, blue error bars) confirm d^3 scaling (solid line fit) rather than d^6 scaling (dashed line fit). Panels (a−c) adapted with permission from ref 66. Copyright 2022 American Chemical Society. Panel (g) adapted with permission from ref 54. Copyright 2019 American Chemical Society.

https://doi.org/10.1021/acs.jpcc.4c05878
J. Phys. Chem. C XXXX, XXX, XXX−XXX

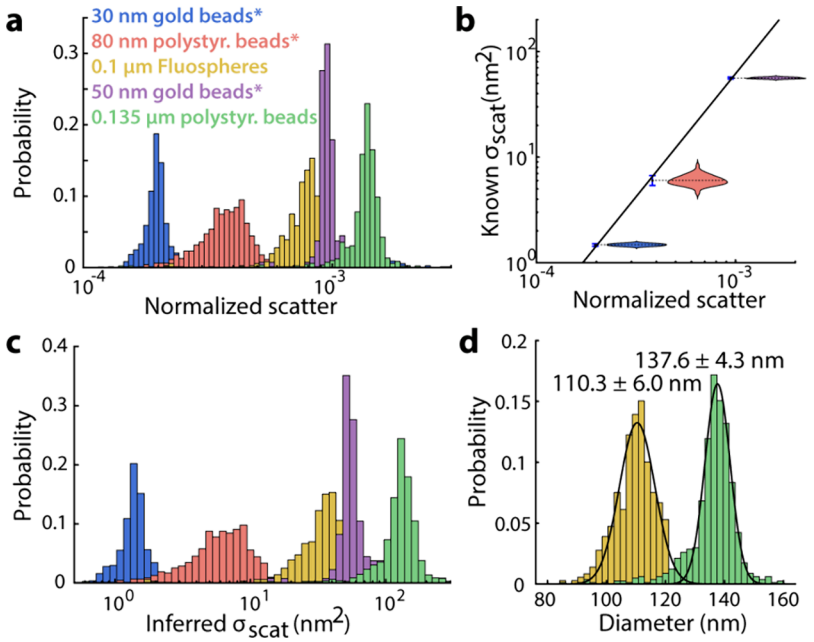

Figure 3. Calibrating normalized scatter to the scattering cross section for single nanoparticles. (a) Measured scattering levels on a series of gold and polystyrene beads, normalized for reflectivity. (b) Power law fit to the 30 nm gold beads, 80 nm polystyrene beads, and 50 nm gold beads to create a calibration to the scattering cross section. (c) Measurements from (a) converted to single-particle scattering cross sections. (d) Two polystyrene bead samples from (c) not used for calibration converted to single-particle diameters. The diameters as measured by TEM are 108 ± 6 and 130 ± 2.4 nm. Figure adapted with permission from ref 60. Copyright 2022 American Chemical Society.

$$C_f = \left| \frac{S_{det} - S_{bkg}}{S_{bkg}} \right| \quad (2)$$

In one simple implementation of a feedback algorithm, the point of the largest scattering contrast is taken as the approximate location of the particle so that a proportional restoring force can be applied in the direction of the trap center (Figure 2d, left). The confining effect of the applied x and y voltages may be confirmed on a subsequent scan (Figure 2d, right).[54]

The presence or absence of a trapped particle may be monitored using the maximum scattering contrast present in any given scan; when particles are absent, the scattering contrast matches background levels, but when a particle enters the trap, the maximum scattering contrast rises sharply (Figure 2e,f). The three peaks arise from a mixture of three different sizes of gold beads with diameters of 20, 30, and 50 nm. Due to the sensitivity of an interferometric scattering signal to the phase of the interference term and therefore sensitivity to the exact x, y, and z positions of the trapped particle relative to the focus, this signal is noisy. Nevertheless, filtering and level finding clearly illustrate that each trapped particle exhibits a characteristic average iSCAT contrast, which is proportional to its volume ($\sim d^3$) as expected (Figure 2g). Using only interferometric scattering to guide closed-loop trapping feedback, the original ISABEL trap was able to confine gold nanoparticles of <20 nm diameter in free solution, removing key requirements for strong target fluorescence that can constrain ABEL trap samples.[54]

3. EXTRACTING THE SCATTERING CROSS SECTION BY CALIBRATING FRACTIONAL CONTRAST

The interferometric scattering scaling with particle polarizability raises the possibility of measuring the masses of single particles and even single proteins, following the success of both mass photometry by interferometric scattering[43,55] and nanofluidic scattering microscopy (NSM).[50] The ISABEL trap offers an additional benefit: since single-nanoparticle masses can be measured without any labeling and by moving scattering to the near infrared, the entire visible spectrum is available for complementary fluorescence measurements (see Section 4). This provides an advantage over the mechanical oscillator/cantilever and electron microscopy-based single-particle mass measurements, which are difficult to multiplex with other modalities.[56−59] The aqueous environment coupled with long observation times also allows for repeated measurements of both scattering and fluorescence variables for increased precision.

For sufficiently small particles in the ISABEL trap (typically a few times smaller than the wavelength), the scattering process can be fully characterized by the scattering cross section of the particle. Compared to typical single-protein mass measurements with iSCAT, which calibrate contrast directly against the mass of the scattering protein, the ISABEL scattering signal is additionally normalized for the reflectivity of the surface and then calibrated against the known scattering cross sections of polystyrene and gold nanoparticles of defined compositions and measured sizes (Figure 3a).[60] This generates a conversion from measured scattering signal to the single-particle scattering cross section in the form of a power law (Figure 3b). The scattering cross section scales approximately as the square of the signal, reflecting the fact that the interferometric scattering contrast is linear in the scattered field. This measurement can be used to convert the scattering signal to inferred scattering cross sections (Figure 3c), and the samples not used for calibration can be used to verify the performance by converting to single-particle diameters with the well-characterized material refractive index and comparing

https://doi.org/10.1021/acs.jpcc.4c05878
J. Phys. Chem. C XXXX, XXX, XXX−XXX

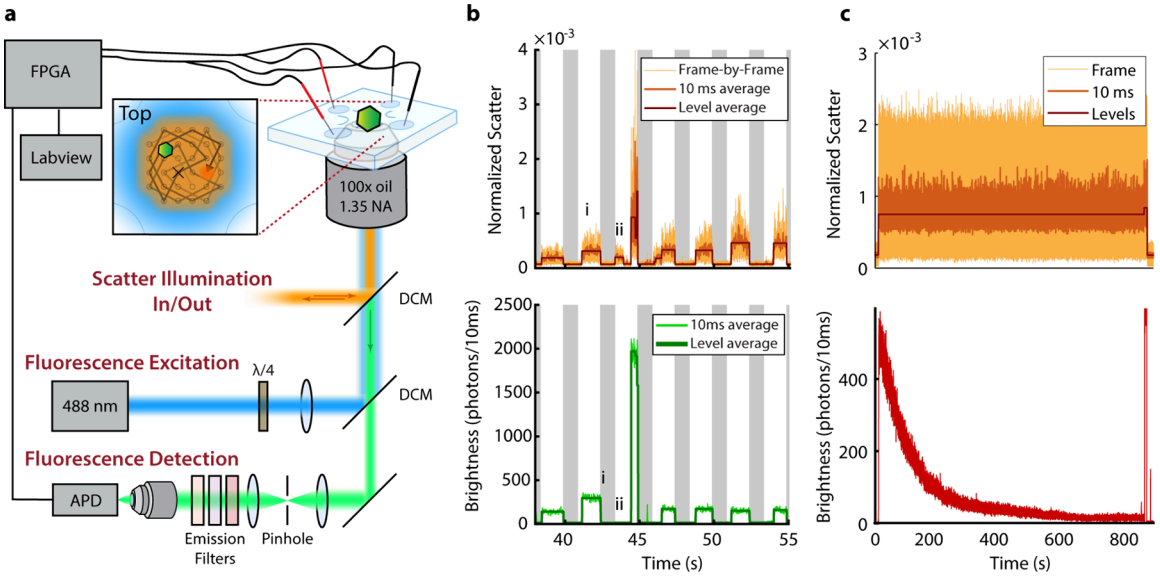

Figure 4. (a) Optical diagram of an augmented ISABEL trap that incorporates simultaneous fluorescence spectroscopy. Wide-field fluorescence excitation illumination is spatially overlapped via dichroic mirrors (DCM) with the knight's tour scan pattern used to detect scattering particles. Emitted fluorescence is spatially filtered through a pinhole, spectrally purified, and detected on an avalanche photodiode (APD). (b) Example trapping trace from carboxysome nanoparticles (see below), highlighting simultaneous scattering and fluorescence information. Carboxysomes are observed to enter the ROI and become trapped one at a time when the feedback is on (white background), causing a sharp step up in both scattering contrast (orange) and fluorescence (green). Contrast remains high during trapping and returns to the background level upon switching off the feedback (gray background). (c) A single 100 nm polystyrene bead labeled with Alexa Fluor 647 is trapped stably for nearly 15 min, even though the fluorescence photobleaches over time. The trapped bead is replaced with a bead with larger contrast and unbleached fluorophores. Panel (b) adapted with permission from ref 60. Copyright 2022 American Chemical Society.

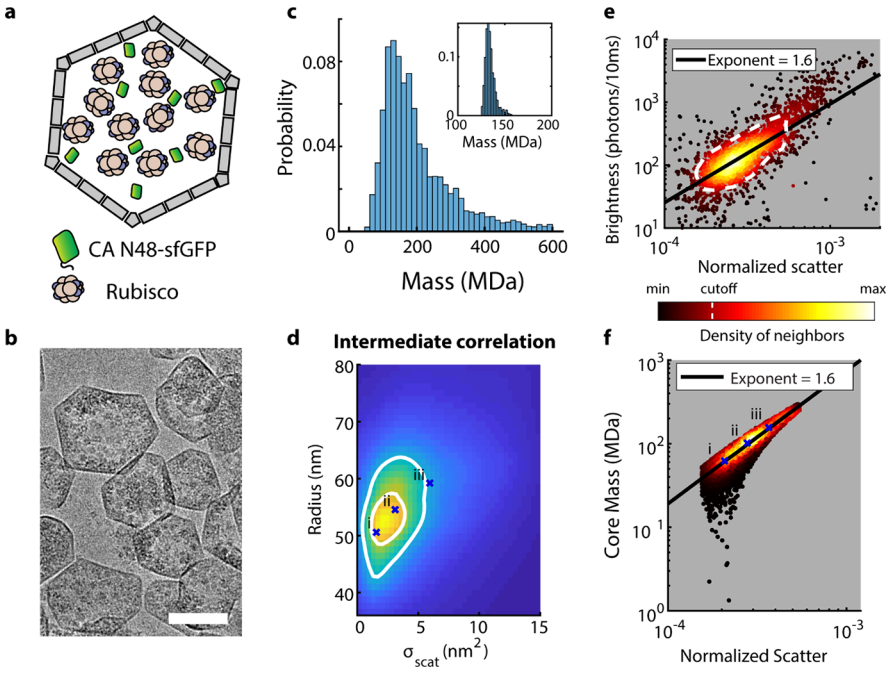

Figure 5. Measuring carboxysome masses and mass distribution. (a) Schematic of the trapped carboxysomes expressed in *E. coli*, with superfolder GFP targeted to the core. (b) Cryo-TEM images of the carboxysomes reveal heterogeneity of size and loading. Scale bar: 100 nm. (c) Distribution of masses inferred from carboxysome trapping data, assuming no correlation between the measured scattering and assumed diameter. Inset: histogram of mass estimates from a single carboxysome. (d) Ensemble of simulated carboxysomes with an intermediate correlation between the radius and the scattering cross section. (e) Measured distribution of fluorescence and normalized scatter for the carboxysome trapping data. The points are colored by local density of neighbors, and points above a cutoff of density (white dashed line) are fit to a power law to characterize the shape, with an exponent of 1.6. (f) Distribution of core mass vs normalized scatter calculated for the ensemble in (d), where the correlation was chosen such that the power law fit matches the exponent from (e). Figure adapted with permission from ref 60. Copyright 2022 American Chemical Society.

https://doi.org/10.1021/acs.jpcc.4c05878
J. Phys. Chem. C XXXX, XXX, XXX−XXX

these results to those measured from electron microscopy of the same samples (Figure 3d).

4. SIMULTANEOUS SCATTERING AND FLUORESCENCE REPORTING

Recent work has demonstrated the advantages of combined scattering and fluorescence microscopy.[61−63] For instance, fluorescence labeling provides a way to introduce species selectivity since scattering is generated regardless of object identity. After the first demonstration of the ISABEL trap,[54] we shifted interferometric scattering detection to 800 nm in the near IR to allow simultaneous monitoring with fluorescence. In addition to the optical path shown in Figure 2a, we introduced wide-field fluorescence excitation at various wavelengths (405, 488, 561, and 638 nm) spatially overlapped with the knight's tour confocal scan for scattering detection (Figure 4a, only one excitation wavelength illustrated here). Fluorescence emission was spectrally separated, spatially filtered through a pinhole, and collected on avalanche photodiodes. In Figure 4b, we show data from individual trapped carboxysomes with internalized superfolder GFP (sfGFP), which is pumped by 488 nm to provide fluorescence. We see that along with scattering, many trapping events simultaneously show fluorescence, such as in event i, confirming that the object is indeed a carboxysome. Conversely, residual impurities (such as the object trapped in event ii) do not display fluorescence and can be separated later in data analysis. Intentional fluorescent reporter design also introduces a means to selectively probe specific nanoparticle regions (Section 5) or infer internal chemistry via spectroscopic reporting (Section 6). Finally, this configuration recovers the ABEL trap's capability for parallelized time-resolved fluorescence spectroscopy. However, by removing fluorescence for localization as in previous ABEL traps, this expands the reporter palette since signal/background requirements are less stringent.

While fluorescence aids specificity, it comes with the inevitability of photobleaching. In Figure 4c, we show a trace from a single trapped polystyrene bead that has been surface-labeled with Alexa Fluor 647. Because the scattering wavelength is nonresonant with the bead's electronic transitions, the scattering signal maintains the same average value over the nearly 15 min of trapping, while the fluorescent labels photobleach even with weak illumination (~1 W/cm^2). In this example, we also see that the original particle is lost only when a larger object (with fresh fluorophores) replaces it at the very end of the trace shown. This supports the notion that in principle, a particle can be localized and trapped indefinitely via interferometric scattering.

5. SINGLE-NANOPARTICLE MASS MEASUREMENTS WITH CARBOXYSOMES

The carboxysome presents a rich target for ISABEL trap experiments and measurements of the masses. The carboxysome is a self-assembled bacterial microcompartment, with hundreds of copies of the enzyme rubisco colocalized with the enzyme carbonic anhydrase, all encapsulated within a semipermeable protein shell ~100 nm in diameter (Figure 5a,b).[64] We obtained carboxysomes heterologously expressed in *Escherichia coli* (*E. coli*) with an sfGFP variant targeted to the interior. Carboxysomes were held in the ISABEL trap with near-IR illumination for interferometric scattering combined with 488 nm excitation for GFP fluorescence. By cycling feedback on and off, a set of individual carboxysomes can be trapped, and the heterogeneity can be sampled. Trapping events are identified with level finding as described in Figure 2 above, and true carboxysome trapping events can be identified by a combination of the presence of fluorescence and scattering signal in an appropriate range.

The measured scattering signals can be converted to scattering cross sections with the calibration described above and converted to single-particle masses with additional modeling (Figure 5c).[60] The carboxysome can be approximated as a spherical protein shell around a protein core with each of the components modeled as an averaged density or refractive index. The density of the protein can be converted to a refractive index, and using structural studies, the carboxysome can be modeled with two free parameters: the total diameter and the core refractive index. For these experiments, the total diameter distribution was measured separately from the ISABEL trapping by cryo-TEM, and it was used to inform the single carboxysome masses. We took two approaches to calculating the carboxysome masses. In the first approach, the diameter was assumed to not be correlated to the scattering cross sections. For any measured scattering cross section, core densities were calculated with the full distribution of diameters, giving a probability distribution of the mass for each carboxysome.

In a second approach,[60] we used the fluorescence signal to constrain the carboxysome models and obtain higher confidence for the underlying parameters. The key insight here is that the scaling of fluorescence vs scattering signal informs us about the relative contribution of the fluorescent core and nonfluorescent shell to the total mass. We generated correlated distributions of the scattering cross section and the total diameter (Figure 5d), parametrized by the degree of correlation, and generated ensembles of carboxysomes with scattering signals and fluorescence, assuming fluorescence proportional to the mass of material in the core. We selected the ensemble (correlation) where the power law fit to simulated fluorescence versus scattering signal (Figure 5f) best matches the measurement on the carboxysome sample of interest (Figure 5e).

The combination of these experiments gives us a picture of carboxysome heterogeneity, combining both the total mass and core loading. The mass distribution is peaked at 130 MDa and ranges between 100 and 250 MDa with ~10% variance for a given single-particle mass (Figure 5c). These single-particle measurements complement other estimates of the mass of carboxysomes: measurements based on counting the relative abundance of proteins are typically limited to ensemble averages. Mass measurements with scanning TEM are limited to samples frozen in vitreous ice with no possibility of measuring dynamics simultaneously and limitations on determining the composition of the particles. Meanwhile, counting proteins in individual carboxysomes in cryo-TEM cannot resolve many of the smaller unstructured proteins that contribute to the carboxysome mass. This application demonstrates the power of the ISABEL trap to combine interferometric scattering-based single-particle mass measurements with correlated fluorescence measurements. Ongoing work entails simultaneous radius estimation in the ISABEL trap either from the feedback needed to suppress lateral diffusion or from axial diffusion, estimated by analyzing time-dependent fluctuations in the (signed) contrast. Better estimates of the single-particle radius along with the single-

https://doi.org/10.1021/acs.jpcc.4c05878
J. Phys. Chem. C XXXX, XXX, XXX−XXX

particle mass will enable closer scrutiny of the density and arrangement of mass within each carboxysome.

6. REDOX SENSING WITH RATIOMETRIC FLUORESCENCE INSIDE SINGLE TRAPPED CARBOXYSOMES

As described in Section 4, shifting the scattering illumination beam to the near-infrared region opens the visible region (~400−750 nm) for flexible fluorescence reporting (Figure 4). This enables us to monitor biochemical status and dynamic chemical changes in and around single nanoparticles, using the many existing fluorescent biosensors that respond to small-molecule species.[65] We recently took advantage of this capability to monitor the redox environment inside individual carboxysomes.[66] Redox chemistry is being increasingly appreciated as necessary for regulating carboxysome formation and carbon concentration activity by carbonic anhydrase (CA).[67−70] Given that carboxysome assemblies are structurally heterogeneous, particularly when expressed recombinantly in *E. coli*,[64] we wanted to explore how structural variation could impact chemical heterogeneity, for example, by heterogeneity in shell permeability. Therefore, we set out to measure the redox properties inside individual carboxysomes (Figure 6a). Compared to the experiments from Section 5, we examined carboxysomes with responsiveness to the introduced reductant.

These trapping experiments were enabled using simultaneous near-IR scattering for carboxysome detection and fluorescence from an internalized redox-sensitive GFP mutant. The redox reporter, roGFP2,[71,72] is an example of a ratiometric fluorescence excitation reporter (Figure 6b), where the excitation spectrum changes in response to the redox environment. To internally reference the signal (Figure 6c), we took the ratio of the brightnesses in the green band (500−570 nm) upon excitation with two wavelengths, here 405 and 488 nm. In this scheme, high fluorescence ratios indicated oxidizing environments, low ratios arose from reducing environments inside the carboxysome, and ratios can be converted to redox potentials.[49] While trapping a carboxysome, we employed alternating excitation and tagged each detected photon with its excitation channel.

This dual-channel fluorescence scheme incorporated into the ISABEL trap provided both scattering and spectroscopic characterization of individual carboxysomes (in 1 mM TCEP, Figure 7a). For a given trapping event, the scattering level reported on the carboxysome's size, while the 405 and 488 nm fluorescence excitation levels encoded the redox information. With the long observation times afforded by trapping, we achieved reasonably precise estimates of the fluorescence brightness in each channel. This was particularly important in the 405 nm channel, where signal/background and signal/noise were both especially low. These multiparameter measurements could be visualized as a series of two-dimensional scatter plots showing the fluorescence ratio $R_{405/488}$ versus the carboxysome scattering contrast (Figure 7b). The ratios for reduced carboxysomes all trend around the same central value, demonstrating the benefit of self-referenced ratiometric signals.

When we trapped carboxysomes in an oxidizing environment, we found that the ratios trend to higher values, as expected, but there was also an unexpectedly large spread in the ratiometric fluorescence (Figure 7c). We ruled out potential sources of extraneous heterogeneity and demonstrated with sfGFP-loaded carboxysomes that ratiometric

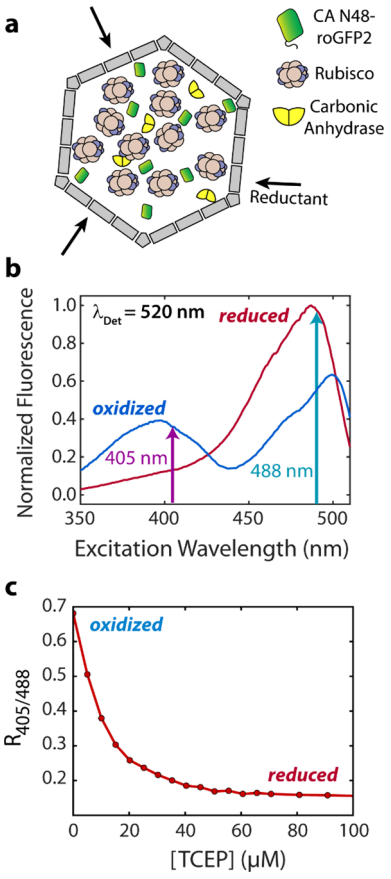

Figure 6. (a) Schematic of a carboxysome with internal roGFP2. (b) Bulk fluorescence excitation spectra from roGFP2 demonstrate changes in the fluorescence with redox conditions. Vertical arrows indicate the excitation wavelengths used in this study. (c) The bulk ratiometric fluorescence readout from roGFP2 decreases with the added reductant. Figure adapted with permission from ref 66. Copyright 2022 American Chemical Society.

fluorescence could be measured with high precision (Figure 7d). This left us to propose that peptides inside the carboxysome interfere with the ratiometric fluorescence of the internalized roGFP2, perhaps due to intermolecular cross-linking. Each roGFP2 protein derives its redox sensitivity via an engineered pair of surface cysteine residues, whose redox-dependent configuration modulates the chromophore's fluorescence excitation spectrum. We hypothesize that there is a probability for either of these cysteines to form disulfide bonds with cysteines on other proteins inside the carboxysome. With the low copy number of roGFP2 in each carboxysome (N_{GFP} ~ 3−15), we could expect a wide variation of the ratiometric response between carboxysomes. With a higher fluorophore copy number, we would expect these effects to average out and produce a narrower redox response, suggested by the narrowed ratiometric response in carboxysome dimers. Together, these experiments have revealed intriguing behavior underscoring the sensitivity of fluorescence reporters to their surrounding molecular environment.

Finally, we used redox sensitivity to investigate the kinetics of small-molecule reductants crossing the shell into carboxysomes. Small reductants such as glutathione (307 Da), DTT (154 Da), and TCEP (250 Da) are smaller than typical organic fluorophores (~1 kDa), so fluorescently labeling the reductants themselves would perturb the entry kinetics.

https://doi.org/10.1021/acs.jpcc.4c05878
J. Phys. Chem. C XXXX, XXX, XXX−XXX

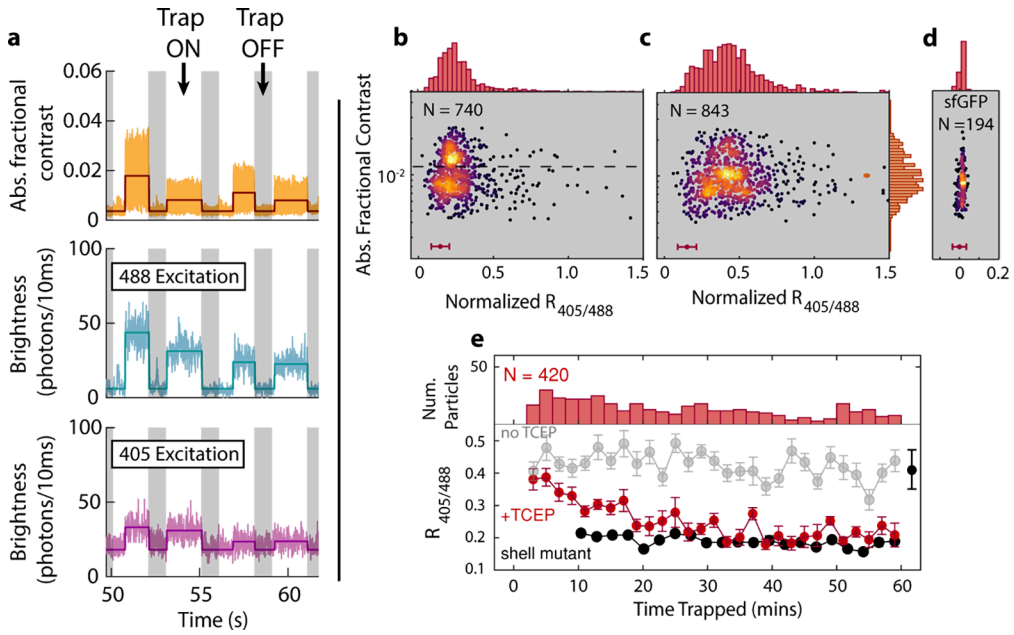

Figure 7. (a) Example carboxysome trapping trace where scattering contrast (top), fluorescence from 488 nm excitation (middle), and fluorescence from 405 nm excitation (bottom) are collected simultaneously from each particle. For each trace, average signal levels are superimposed over trapping events. (b) Ratiometric fluorescence and scattering contrast measured for carboxysomes in highly reducing conditions (1 mM TCEP). The error bar indicates the RMS standard error on ratio measurements. (c) Ratiometric fluorescence and scattering contrast for air-oxidized carboxysomes. (d) Ratiometric fluorescence for carboxysomes loaded with sfGFP, which is insensitive to redox. The measured ratios all lie within measurement error (red bar). (e) Upon mixing air-equilibrated roGFP2-carboxysomes with a reducing buffer, the ratiometric fluorescence decreases demonstrate the minutes-long kinetics for small-molecule reductants to enter the carboxysome. Panels (a–d) adapted with permission from ref 66. Copyright 2022 American Chemical Society. With the exception of shell mutant data, panel (e) is also adapted with permission from ref 66. Copyright 2022 American Chemical Society.

However, by introducing roGFP2 into the interior, we could track the reduction inside the carboxysome once small molecules had entered. We mixed air-oxidized carboxysomes with a reducing solution, quickly loaded the mixture into the trap, and trapped many individual carboxysomes for ∼1 s each over the course of an hour. Figure 7e shows that carboxysomes are internally reduced on a roughly 15 min timescale, consistent with subsequent work monitoring other small molecules permeating carboxysomes.[73] To confirm that this timescale is limited by the shell and not the kinetics of roGFP2, we also reduced carboxysomes with the shell pentamer knockout ΔCsoS4,[74] introducing open gaps at the carboxysome shell vertices. These carboxysomes with porous shells displayed full internal reduction at the initial measured time point, demonstrating that the minutes-long internal reduction of intact carboxysome resulted from a kinetic barrier imposed by an intact shell.

7. DISCUSSION AND OUTLOOK

The experiments presented here demonstrate the utility of the ISABEL trap to sense multiple properties from individual nanoparticles in solution with a high precision. With a straightforward calibration of the scattering, single-particle mass measurements can be achieved, and fluorescence can report on compartment loading or the redox environment. As shown by trapping "ultrauniform" gold nanoparticles in Figure 2f, extended measurement of scattering provides highly precise estimates of single-particle contrast, producing narrow contrast histograms. Additionally, ISABEL robustly traps single nanoparticles for several minutes (Figure 4c), in principle only limited by replacement by larger particles, the frequency of which can be tuned by adjusting the sample concentration. On top of these capabilities, strengths of the traditional ABEL trap can also apply here, such as using feedback statistics to estimate a particle's diffusion coefficient and electrokinetic mobility[28,29] or using time-resolved fluorescence for fluorescence lifetime and anisotropy.[22] These sensing capabilities can be obtained either from single fluorophores within a trapped nanoparticle or with multiple reporters producing a small ensemble-averaged fluorescence from a single object for higher brightness.

For single nanoparticles, detection by interferometric scattering overcomes many of the limitations of fluorescence-based particle localization. Chief among these limitations is that fluorescence is not universal so that particle detection has required either intrinsic fluorescence or the chemical attachment of an emissive label. Also, the inherently finite photon budget[75] of an organic fluorophore ensures that a labeled object cannot be trapped indefinitely. Furthermore, long-term trapping requires the use of strong emitters, i.e., those with high brightness and no blinking, typically requiring solution additives for oxygen scavenging and triplet quenching.[27] Finally, the environment around the single object must produce minimal background photons, which introduce false-positive detections that can throw off feedback.[76] For nanoscale biomolecular objects labeled with a bright organic fluorophore such as Alexa Fluor 647, trapping times can extend to a few tens of seconds, though trapping times are more typically in the 100 ms or few-second regime. At the same time, interferometric scattering requires objects of sufficient size to generate a detectable scattering signal, and the best way

https://doi.org/10.1021/acs.jpcc.4c05878
J. Phys. Chem. C XXXX, XXX, XXX−XXX

to detect and trap single small organic molecules remains to be fluorescence.[27]

By delegating particle position estimation to scattering, one can significantly relax the constraints described above to design more flexible fluorescence spectroscopic schemes. Additional fluorescence reporting has already provided many advantages to scattering-based particle detection, with more capabilities within reach. First, since interferometric scattering is not a specific phenomenon, fluorescence detection provides a way to confirm the identity of a particular trapped particle, which has proven useful in identifying trapped particles as in Figure 4b. Also, intentional fluorescent reporter design introduces a means to selectively probe specific nanoparticle regions (Section 5) or infer internal chemistry via spectroscopic reporting (Section 6). As seen in Figure 7a, the 405 nm-excited fluorescence exhibits low signal and high background but does not impede the trapping ability. Also, intermittent fluorescence excitation can be employed to monitor the progress of slow kinetics (e.g., accumulation of a labeled protein) while mitigating photobleaching. Finally, pulsed fluorescence excitation recovers the capability for parallelized time-resolved fluorescence spectroscopy like in the ABEL trap. Recent advances in nanoflow cytometry with spectral measurement corroborate the advantages of combining fluorescence and scattering measurements on single biological nanoparticles for multivariate characterization.[77]

Importantly, while the ABEL trap was optimized with single-molecule spectroscopy in mind, there are exciting and useful developments for the ISABEL trap for the study of heterogeneous nanoparticle samples. In particular, the scattering amplitude of a single trapped nanoparticle can be used for precise refractive index sensing, where this might be helpful in determining the composition of complicated biological samples such as extracellular vesicles, which contain a mix of lipids and proteins.[44] Also, the fluctuations of the scattering contrast reflect diffusion in the axial direction where we physically confine the sample in a microfluidic channel. The high sensitivity of the z position inherent to interferometric scattering could be exploited as an orthogonal measurement of the hydrodynamic radius. The electrokinetic mobility measured from a single particle can be converted to its zeta potential, commonly characterized in novel nanoparticles, and reflects the presence of charged species around the particle's surface.[78] Changes in electrokinetic mobility can also report on changes in the particle charge state.[29] Long-term label-free trapping enables the following of each of these parameters in time, which could be used to monitor the slow release of molecular cargos, for example.

While there is now a wide variety of techniques for direct detection of single nanoparticles, the design of the ISABEL trap uniquely positions it to complement label-free observation and sensing of scattering properties with time-resolved fluorescence spectroscopic reporting. For instance, label-free single-particle tracking measurements have demonstrated sensitivity to particle polarizability and hydrodynamic radius.[45,50] With kHz frame rates,[45] even subsecond tracks can produce impressive estimates of the particle's hydrodynamic radius without trapping. For comparison, the parallelized high-throughput characterization afforded by CLiC microscopy allows the facile collection of particle statistics using wide-field fluorescence detection on a scientific camera.[32] The trade-off with camera-based detection methods is the limited frame rate (~50 fps)[34] and inaccessibility of time-resolved fluorescence spectroscopy. To compare to another technique with point detection, RT-3D-SPT is distinct in its ability for deep axial observation and for its ability to follow a fluorescent nanoparticle through *in vivo* conditions,[31] even if it is limited by the feedback speed of the stage to objects with diffusion coefficients of ~10 $\mu m^2/s$.[79] Conversely, the design of anti-Brownian traps has demonstrated a trapping ability for single small molecules with diffusion coefficients up to 300 $\mu m^2/s$, and active feedback statistics allow recovery of not only the diffusion coefficient but also the electrophoretic mobility.[27,29] Finally, single fluorescent photon detection by APDs interfaced with time-correlated single-photon counting (TCSPC) allows for ns-timescale measurements on single objects.[27] Access to these distinct properties gives ISABEL a unique and complementary role to those of other techniques in single-particle biophysical studies.

The capabilities enabled by the ISABEL trap open up new types of experiments, revealing variation and single-particle reaction dynamics involving single biomolecular nanoparticles. Work is currently underway to continue exploration of the shells of single carboxysomes. Also, the minutes-long trapping affords us the ability to track slow processes like the formation of a protein corona around a particular nanoparticle or the release of a therapeutic payload from new drug delivery nanoparticles. Various types of biocompatible drug delivery nanoparticles such as polyplexes and RNA LNPs have provided new ways of delivering genetic material into the cell, and understanding the biophysical principles for particle formation[34] and cargo delivery[80] is an active area of research. Finally, trapping enables the detailed and multifaceted characterization of individual viruses and virus-like particles, where the heterogeneity of enveloped components and nucleic acid loading is a key concern. Flexible characterization of extracellular vesicles and their various constituents can provide new measurements in the search for reliable diagnostic markers. All of these ideas may also have parallels in nonbiological nanoparticles as well.

Trapping individual nanoparticles enables a distinct and detailed look at each object, revealing variation between individuals and using that to gain deeper insight into the organization and self-assembly principles for each class of objects. This detailed look, in the form of a multiplexed readout and long observation time, plays a distinct role in single-particle spectroscopy. The experiments demonstrated here show just a few examples of the technique's capability, with further updates within reach. Combining the best of label-free particle characterization with spectroscopy afforded by fluorescence reporting provides simultaneous nanoscale and molecular-scale data on each particle. This rich characterization will be well-positioned to provide clarity on how to engineer biomolecular nanoparticles for addressing global challenges in the coming decades.

AUTHOR INFORMATION

Corresponding Author

W. E. Moerner − *Department of Chemistry and Department of Applied Physics, Stanford University, Stanford, California 94305, United States;* orcid.org/0000-0002-2830-209X; Email: wmoerner@stanford.edu

Authors

William B. Carpenter − *Department of Chemistry, Stanford University, Stanford, California 94305, United States;*

https://doi.org/10.1021/acs.jpcc.4c05878
J. Phys. Chem. C XXXX, XXX, XXX−XXX

Present Address: Department of Chemistry and Biochemistry, The Ohio State University, Columbus,Ohio 43210, United States; orcid.org/0000-0002-6174-1035

Abhijit A. Lavania − *Department of Applied Physics, Stanford University, Stanford, California 94305, United States;* Present Address: Double Helix Optics, Boulder, Colorado 80303, United States; orcid.org/0000-0002-8873-0184

Allison H. Squires − *Pritzker School of Molecular Engineering and Institute for Biophysical Dynamics, University of Chicago, Chicago, Illinois 60637, United States; Chan Zuckerberg Biohub Chicago, LLC, Chicago, Illinois 60642, United States;* orcid.org/0000-0002-2417-1432

Complete contact information is available at: https://pubs.acs.org/10.1021/acs.jpcc.4c05878

Notes

The authors declare no competing financial interest.

■ ACKNOWLEDGMENTS

This work was supported in part by the U.S. Department of Energy, Office of Science, Office of Basic Energy Sciences, Chemical Sciences, Geosciences, & Biosciences Division, Physical Biosciences Program, under Award Number DE-FG02-07ER15892 (W.E.M.) and Award Number DE-SC0025385 (A.H.S.). A.H.S. acknowledges support from the Neubauer Family Foundation.

■ REFERENCES

(1) Zijlstra, P.; Paulo, P. M. R.; Orrit, M. Optical detection of single non-absorbing molecules using the surface plasmon resonance of a gold nanorod. *Nat. Nanotechnol.* **2012**, *7*, 379−382.

(2) Mitchell, M. J.; Billingsley, M. M.; Haley, R. M.; Wechsler, M. E.; Peppas, N. A.; Langer, R. Engineering precision nanoparticles for drug delivery. *Nat. Rev. Drug Discovery* **2021**, *20*, 101−124.

(3) Liu, L.; Corma, A. Metal Catalysts for Heterogeneous Catalysis: From Single Atoms to Nanoclusters and Nanoparticles. *Chem. Rev.* **2018**, *118*, 4981−5079.

(4) Kirst, H.; Ferlez, B. H.; Lindner, S. N.; Cotton, C. A. R.; Bar-Even, A.; Kerfeld, C. A. Toward a glycyl radical enzyme containing synthetic bacterial microcompartment to produce pyruvate from formate and acetate. *Proc. Natl. Acad. Sci. U.S.A.* **2022**, *119*, No. e2116871119.

(5) Aharonovich, I.; Castelletto, S.; Simpson, D. A.; Su, C. H.; Greentree, A. D.; Prawer, S. Diamond-based single-photon emitters. *Rep. Prog. Phys.* **2011**, *74*, No. 076501.

(6) Dolde, F.; Fedder, H.; Doherty, M. W.; Nöbauer, T.; Rempp, F.; Balasubramanian, G.; Wolf, T.; Reinhard, F.; Hollenberg, L. C. L.; Jelezko, F.; et al. Electric-field sensing using single diamond spins. *Nat. Phys.* **2011**, *7*, 459−463.

(7) Stavis, S. M.; Fagan, J. A.; Stopa, M.; Liddle, J. A. Nanoparticle Manufacturing − Heterogeneity through Processes to Products. *ACS Appl. Nano Mater.* **2018**, *1*, 4358−4385.

(8) Berne, B. J.; Pecora, R. *Dynamic Light Scattering: With Applications to Chemistry, Biology, and Physics*; Dover: Mineola, NY, 2000.

(9) Yu, L.; Lei, Y.; Ma, Y.; Liu, M.; Zheng, J.; Dan, D.; Gao, P. A Comprehensive Review of Fluorescence Correlation Spectroscopy. *Front. Phys.* **2021**, *9*, No. 644450.

(10) Gallego-Urrea, J. A.; Tuoriniemi, J.; Hassellöv, M. Applications of particle-tracking analysis to the determination of size distributions and concentrations of nanoparticles in environmental, biological and food samples. *TrAC, Trends Anal. Chem.* **2011**, *30*, 473−483.

(11) Chakraborty, M.; Kuriata, A. M.; Henderson, J. N.; Salvucci, M. E.; Wachter, R. M.; Levitus, M. Protein Oligomerization Monitored by Fluorescence Fluctuation Spectroscopy: Self-Assembly of Rubisco Activase. *Biophys. J.* **2012**, *103*, 949−958.

(12) Wang, Q.; Serban, A. J.; Wachter, R. M.; Moerner, W. E. Single-molecule diffusometry reveals the nucleotide-dependent oligomerization pathways of Nicotiana tabacum Rubisco activase. *J. Chem. Phys.* **2018**, *148*, 123319.

(13) Patois, E.; Capelle, M. A. H.; Palais, C.; Gurny, R.; Arvinte, T. Evaluation of nanoparticle tracking analysis (NTA) in the characterization of therapeutic antibodies and seasonal influenza vaccines: pros and cons. *J. Drug. Delivery Sci. Technol.* **2012**, *22*, 427−433.

(14) Filipe, V.; Hawe, A.; Jiskoot, W. Critical Evaluation of Nanoparticle Tracking Analysis (NTA) by NanoSight for the Measurement of Nanoparticles and Protein Aggregates. *Pharm. Res.* **2010**, *27*, 796−810.

(15) Cohen, A. E.; Moerner, W. E. Suppressing Brownian motion of individual biomolecules in solution. *Proc. Natl. Acad. Sci. U.S.A.* **2006**, *103*, 4362−4365.

(16) Squires, A. H.; Cohen, A. E.; Moerner, W. E., Anti-Brownian Traps. In *Encyclopedia of Biophysics*; Roberts, G. C. K.; Watts, A., Eds. Springer: Berlin, Heidelberg, 2018.

(17) Bespalova, M. I.; Mahanta, S.; Krishnan, M. Single-molecule trapping and measurement in solution. *Curr. Opin. Chem. Biol.* **2019**, *51*, 113−121.

(18) Cohen, A. E.; Moerner, W. E. Principal-components analysis of shape fluctuations of single DNA molecules. *Proc. Natl. Acad. Sci. U.S.A.* **2007**, *104*, 12622−12627.

(19) Jiang, Y.; Douglas, N. R.; Conley, N. R.; Miller, E. J.; Frydman, J.; Moerner, W. E. Sensing cooperativity in ATP hydrolysis for single multisubunit enzymes in solution. *Proc. Natl. Acad. Sci. U.S.A.* **2011**, *108*, 16962−16967.

(20) Squires, A. H.; Dahlberg, P. D.; Liu, H.; Magdaong, N. C. M.; Blankenship, R. E.; Moerner, W. E. Single-molecule trapping and spectroscopy reveals photophysical heterogeneity of phycobilisomes quenched by Orange Carotenoid Protein. *Nat. Commun.* **2019**, *10*, 1172.

(21) Squires, A. H.; Moerner, W. E. Direct single-molecule measurements of phycocyanobilin photophysics in monomeric C-phycocyanin. *Proc. Natl. Acad. Sci. U.S.A.* **2017**, *114*, 9779−9784.

(22) Squires, A. H.; Wang, Q.; Dahlberg, P. D.; Moerner, W. E. A bottom-up perspective on photodynamics and photoprotection in light-harvesting complexes using anti-Brownian trapping. *J. Chem. Phys.* **2022**, *156*, No. 070901.

(23) Schlau-Cohen, G. S.; Wang, Q.; Southall, J.; Cogdell, R. J.; Moerner, W. E. Single-molecule spectroscopy reveals photosynthetic LH2 complexes switch between emissive states. *Proc. Natl. Acad. Sci. U.S.A.* **2013**, *110*, 10899−10903.

(24) Wang, Q.; Moerner, W. E. Dissecting pigment architecture of individual photosynthetic antenna complexes in solution. *Proc. Natl. Acad. Sci. U.S.A.* **2015**, *112*, 13880−13885.

(25) Wilson, H.; Wang, Q. ABEL-FRET: tether-free single-molecule FRET with hydrodynamic profiling. *Nat. Methods* **2021**, *18*, 816−820.

(26) Chu, J.; Ejaz, A.; Lin, K. M.; Joseph, M. R.; Coraor, A. E.; Drummond, D. A.; Squires, A. H. Single-molecule fluorescence multiplexing by multi-parameter spectroscopic detection of nanostructured FRET labels. *Nat. Nanotechnol.* **2024**, *19*, 1150.

(27) Wang, Q.; Moerner, W. E. Lifetime and spectrally resolved characterization of the photodynamics of single fluorophores in solution using the Anti-Brownian Electrokinetic Trap. *J. Phys. Chem. B* **2013**, *117*, 4641−4648.

(28) Fields, A. P.; Cohen, A. E. Electrokinetic trapping at the one nanometer limit. *Proc. Natl. Acad. Sci. U.S.A.* **2011**, *108*, 8937−8942.

(29) Wang, Q.; Moerner, W. E. Single-molecule motions enable direct visualization of biomolecular interactions in solution. *Nat. Methods* **2014**, *11*, 555−558.

(30) Welsher, K.; Yang, H. Multi-resolution 3D visualization of the early stages of cellular uptake of peptide-coated nanoparticles. *Nat. Nanotechnol.* **2014**, *9*, 198−203.

(31) Johnson, C.; Exell, J.; Lin, Y.; Aguilar, J.; Welsher, K. D. Capturing the start point of the virus−cell interaction with high-speed 3D single-virus tracking. *Nat. Methods* **2022**, *19*, 1642−1652.

(32) Leslie, S. R.; Fields, A. P.; Cohen, A. E. Convex Lens-Induced Confinement for Imaging Single Molecules. *Anal. Chem.* **2010**, *82*, 6224−6229.
(33) Kamanzi, A.; Gu, Y.; Tahvildari, R.; Friedenberger, Z.; Zhu, X.; Berti, R.; Kurylowicz, M.; Witzigmann, D.; Kulkarni, J. A.; Leung, J.; et al. Simultaneous, Single-Particle Measurements of Size and Loading Give Insights into the Structure of Drug-Delivery Nanoparticles. *ACS Nano* **2021**, *15*, 19244−19255.
(34) Kamanzi, A.; Zhang, Y.; Gu, Y.; Liu, F.; Berti, R.; Wang, B.; Saadati, F.; Ciufolini, M. A.; Kulkarni, J.; Cullis, P.; et al. Quantitative Visualization of Lipid Nanoparticle Fusion as a Function of Formulation and Process Parameters. *ACS Nano* **2024**, *18*, 18191−18201.
(35) Ruggeri, F.; Zosel, F.; Mutter, N.; Rózycka, M.; Wojtas, M.; Ozyhar, A.; Schuler, B.; Krishnan, M. Single-molecule electrometry. *Nat. Nanotechnol.* **2017**, *12*, 488−495.
(36) Braun, M.; Cichos, F. Optically controlled thermophoretic trapping of single nano-objects. *ACS Nano* **2013**, *7*, 11200−11208.
(37) Juan, M. L.; Gordon, R.; Pang, Y.; Eftekhari, F.; Quidant, R. Self-induced back-action optical trapping of dielectric nanoparticles. *Nat. Phys.* **2009**, *5*, 915−919.
(38) Pang, Y.; Gordon, R. Optical Trapping of 12 nm Dielectric Spheres Using Double-Nanoholes in a Gold Film. *Nano Lett.* **2011**, *11*, 3763−3767.
(39) Taylor, R. W.; Sandoghdar, V. Interferometric scattering microscopy: seeing single nanoparticles and molecules via Rayleigh scattering. *Nano Lett.* **2019**, *19*, 4827.
(40) Daaboul, G. G.; Vedula, R. S.; Ahn, S.; Lopez, C. A.; Reddington, A.; Ozkumur, E.; Ünlü, M. S. LED-based Interferometric Reflectance Imaging Sensor for quantitative dynamic monitoring of biomolecular interactions. *Biosens. Bioelectron.* **2011**, *26*, 2221−2227.
(41) Young, G.; Kukura, P. Interferometric Scattering Microscopy. *Annu. Rev. Phys. Chem.* **2019**, *70*, 301−322.
(42) Lindfors, K.; Kalkbrenner, T.; Stoller, P.; Sandoghdar, V. Detection and spectroscopy of gold nanoparticles using supercontinuum white light confocal microscopy. *Phys. Rev. Lett.* **2004**, *93*, No. 037401.
(43) Young, G.; Hundt, N.; Cole, D.; Fineberg, A.; Andrecka, J.; Tyler, A.; Olerinyova, A.; Ansari, A.; Marklund, E. G.; Collier, M. P.; et al. Quantitative mass imaging of single biological macromolecules. *Science* **2018**, *360*, 423.
(44) Kashkanova, A. D.; Blessing, M.; Reischke, M.; Baur, J. O.; Baur, A. S.; Sandoghdar, V.; Van Deun, J. Label-free discrimination of extracellular vesicles from large lipoproteins. *J. Extracell. Vesicles* **2023**, *12*, 12348.
(45) Kashkanova, A. D.; Blessing, M.; Gemeinhardt, A.; Soulat, D.; Sandoghdar, V. Precision size and refractive index analysis of weakly scattering nanoparticles in polydispersions. *Nat. Methods* **2022**, *19*, 586−593.
(46) Foley, E. D. B.; Kushwah, M. S.; Young, G.; Kukura, P. Mass photometry enables label-free tracking and mass measurement of single proteins on lipid bilayers. *Nat. Methods* **2021**, *18*, 1247−1252.
(47) Heermann, T.; Steiert, F.; Ramm, B.; Hundt, N.; Schwille, P. Mass-sensitive particle tracking to elucidate the membrane-associated MinDE reaction cycle. *Nat. Methods* **2021**, *18*, 1239−1246.
(48) Hsieh, C.-L.; Spindler, S.; Ehrig, J.; Sandoghdar, V. Tracking Single Particles on Supported Lipid Membranes: Multimobility Diffusion and Nanoscopic Confinement. *J. Phys. Chem. B* **2014**, *118*, 1545−1554.
(49) Wu, H.-M.; Lin, Y.-H.; Yen, T.-C.; Hsieh, C.-L. Nanoscopic substructures of raft-mimetic liquid-ordered membrane domains revealed by high-speed single-particle tracking. *Sci. Rep.* **2016**, *6*, 20542.
(50) Špačková, B.; Klein Moberg, H.; Fritzsche, J.; Tenghamn, J.; Sjösten, G.; Šípová-Jungová, H.; Albinsson, D.; Lubart, Q.; van Leeuwen, D.; Westerlund, F.; et al. Label-free nanofluidic scattering microscopy of size and mass of single diffusing molecules and nanoparticles. *Nat. Methods* **2022**, *19*, 751−758.
(51) Küppers, M.; Albrecht, D.; Kashkanova, A. D.; Lühr, J.; Sandoghdar, V. Confocal interferometric scattering microscopy reveals 3D nanoscopic structure and dynamics in live cells. *Nat. Commun.* **2023**, *14*, 1962.
(52) Mazaheri, M.; Kasaian, K.; Albrecht, D.; Renger, J.; Utikal, T.; Holler, C.; Sandoghdar, V. iSCAT microscopy and particle tracking with tailored spatial coherence. *Optica* **2024**, *11*, 1030−1038.
(53) Olsén, E.; García Rodríguez, B.; Skärberg, F.; Parkkila, P.; Volpe, G.; Höök, F.; Sundås Midtvedt, D. Dual-Angle Interferometric Scattering Microscopy for Optical Multiparametric Particle Characterization. *Nano Lett.* **2024**, *24*, 1874−1881.
(54) Squires, A. H.; Lavania, A. A.; Dahlberg, P. D.; Moerner, W. E. Interferometric scattering enables fluorescence-free electrokinetic trapping of single nanoparticles in free solution. *Nano Lett.* **2019**, *19*, 4112−4117.
(55) Asor, R.; Kukura, P. Characterising biomolecular interactions and dynamics with mass photometry. *Curr. Opin. Chem. Biol.* **2022**, *68*, No. 102132.
(56) Katsikis, G.; Hwang, I. E.; Wang, W.; Bhat, V. S.; McIntosh, N. L.; Karim, O. A.; Blus, B. J.; Sha, S.; Agache, V.; Wolfrum, J. M.; et al. Weighing the DNA Content of Adeno-Associated Virus Vectors with Zeptogram Precision Using Nanomechanical Resonators. *Nano Lett.* **2022**, *22*, 1511−1517.
(57) Metskas, L. A.; Ortega, D.; Oltrogge, L. M.; Blikstad, C.; Lovejoy, D. R.; Laughlin, T. G.; Savage, D. F.; Jensen, G. J. Rubisco forms a lattice inside alpha-carboxysomes. *Nat. Commun.* **2022**, *13*, 4863.
(58) Sage, E.; Sansa, M.; Fostner, S.; Defoort, M.; Gély, M.; Naik, A. K.; Morel, R.; Duraffourg, L.; Roukes, M. L.; Alava, T.; Jourdan, G.; Colinet, E.; Masselon, C.; Brenac, A.; Hentz, S. Single-particle mass spectrometry with arrays of frequency-addressed nanomechanical resonators. *Nat. Commun.* **2018**, *9*, 3283.
(59) Schmid, M. F.; Paredes, A. M.; Khant, H. A.; Soyer, F.; Aldrich, H. C.; Chiu, W.; Shively, J. M. Structure of Halothiobacillus neapolitanus Carboxysomes by Cryo-electron Tomography. *J. Mol. Biol.* **2006**, *364*, 526−535.
(60) Lavania, A. A.; Carpenter, W. B.; Oltrogge, L. M.; Perez, D.; Turnsek, J. B.; Savage, D. F.; Moerner, W. E. Exploring Masses and Internal Mass Distributions of Single Carboxysomes in Free Solution Using Fluorescence and Interferometric Scattering in an Anti-Brownian Trap. *J. Phys. Chem. B* **2022**, *126*, 8747−8759.
(61) Ortega Arroyo, J.; Cole, D.; Kukura, P. Interferometric scattering microscopy and its combination with single-molecule fluorescence imaging. *Nat. Protoc.* **2016**, *11*, 617−633.
(62) Park, J.-S.; Lee, I.-B.; Moon, H.-M.; Ryu, J.-S.; Kong, S.-Y.; Hong, S.-C.; Cho, M. Fluorescence-Combined Interferometric Scattering Imaging Reveals Nanoscale Dynamic Events of Single Nascent Adhesions in Living Cells. *J. Phys. Chem. Lett.* **2020**, *11*, 10233−10241.
(63) Zheng, Y.; Lim, Y. J.; Lin, H.; Xu, T.; Longbottom, C.; Delghingaro-Augusto, V.; Thong, Y. L.; Parish, C. R.; Gardiner, E. E.; Lee, W. M. Combined Scattering, Interferometric, and Fluorescence Oblique Illumination for Live Cell Nanoscale Imaging. *ACS Photonics* **2022**, *9*, 3876−3887.
(64) Bonacci, W.; Teng, P. K.; Afonso, B.; Niederholtmeyer, H.; Grob, P.; Silver, P. A.; Savage, D. F. Modularity of a carbon-fixing protein organelle. *Proc. Natl. Acad. Sci. U.S.A.* **2012**, *109*, 478.
(65) Greenwald, E. C.; Mehta, S.; Zhang, J. Genetically Encoded Fluorescent Biosensors Illuminate the Spatiotemporal Regulation of Signaling Networks. *Chem. Rev.* **2018**, *118*, 11707−11794.
(66) Carpenter, W. B.; Lavania, A. A.; Borden, J. S.; Oltrogge, L. M.; Perez, D.; Dahlberg, P. D.; Savage, D. F.; Moerner, W. E. Ratiometric Sensing of Redox Environments Inside Individual Carboxysomes Trapped in Solution. *J. Phys. Chem. Lett.* **2022**, *13*, 4455.
(67) Heinhorst, S.; Williams, E. B.; Cai, F.; Murin, C. D.; Shively, J. M.; Cannon, G. C. Characterization of the carboxysomal carbonic anhydrase CsoSCA from Halothiobacillus neapolitanus. *J. Bacteriol.* **2006**, *188*, 8087−8094.

https://doi.org/10.1021/acs.jpcc.4c05878
J. Phys. Chem. C XXXX, XXX, XXX−XXX

(68) Chen, A. H.; Robinson-Mosher, A.; Savage, D. F.; Silver, P. A.; Polka, J. K. The bacterial carbon-fixing organelle is formed by shell envelopment of preassembled cargo. *PLoS One* **2013**, *8*, No. e76127.
(69) Borden, J. S.; Savage, D. F. New discoveries expand possibilities for carboxysome engineering. *Curr. Opin. Microbiol.* **2021**, *61*, 58−66.
(70) Turnsek, J. B.; Oltrogge, L. M.; Savage, D. F. Conserved and repetitive motifs in an intrinsically disordered protein drive α-carboxysome assembly. *J. Biol. Chem.* **2024**, *300*, No. 107532.
(71) Cannon, M.; Remington, S. J. Re-engineering redox-sensitive green fluorescent protein for improved response rate. *Protein Sci.* **2006**, *15*, 45−57.
(72) Hanson, G. T.; Aggeler, R.; Oglesbee, D.; Cannon, M.; Capaldi, R. A.; Tsien, R. Y.; Remington, S. J. Investigating mitochondrial redox potential with redox-sensitive green fluorescent protein indicators. *J. Biol. Chem.* **2004**, *279*, 13044−13063.
(73) Huang, J.; Jiang, Q.; Yang, M.; Dykes, G. F.; Weetman, S. L.; Xin, W.; He, H.-L.; Liu, L.-N. Probing the Internal pH and Permeability of a Carboxysome Shell. *Biomacromolecules* **2022**, *23*, 4339−4348.
(74) Cai, F.; Menon, B. B.; Cannon, G. C.; Curry, K. J.; Shively, J. M.; Heinhorst, S. The Pentameric Vertex Proteins Are Necessary for the Icosahedral Carboxysome Shell to Function as a CO2 Leakage Barrier. *PLoS One* **2009**, *4*, No. e7521.
(75) Moerner, W. E.; Fromm, D. P. Methods of single-molecule fluorescence spectroscopy and microscopy. *Rev. Sci. Instrum.* **2003**, *74*, 3597−3619.
(76) Wang, Q.; Moerner, W. Optimal strategy for trapping single fluorescent molecules in solution using the ABEL trap. *Appl. Phys. B-Lasers O.* **2010**, *99*, 23−30.
(77) Li, L.; Wang, S.; Xue, J.; Lin, Y.; Su, L.; Xue, C.; Mao, C.; Cai, N.; Tian, Y.; Zhu, S.; et al. Development of Spectral Nano-Flow Cytometry for High-Throughput Multiparameter Analysis of Individual Biological Nanoparticles. *Anal. Chem.* **2023**, *95*, 3423−3433.
(78) Smith, M. C.; Crist, R. M.; Clogston, J. D.; McNeil, S. E. Zeta potential: a case study of cationic, anionic, and neutral liposomes. *Anal. Bioanal. Chem.* **2017**, *409*, 5779−5787.
(79) Hou, S.; Exell, J.; Welsher, K. Real-time 3D single molecule tracking. *Nat. Commun.* **2020**, *11*, 3607.
(80) Patel, S.; Ashwanikumar, N.; Robinson, E.; Xia, Y.; Mihai, C.; Griffith, J. P.; Hou, S.; Esposito, A. A.; Ketova, T.; Welsher, K.; Joyal, J. L.; Almarsson, Ö.; Sahay, G.; et al. Naturally-occurring cholesterol analogues in lipid nanoparticles induce polymorphic shape and enhance intracellular delivery of mRNA. *Nat. Commun.* **2020**, *11*, 983.

https://doi.org/10.1021/acs.jpcc.4c05878
J. Phys. Chem. C XXXX, XXX, XXX−XXX